Revealing Soil Structure and Functional Macroporosity along a Clay Gradient Using X-ray Computed Tomography

Muhammad Naveed*
Dep. of Agroecology
Faculty of Science and Technology
Aarhus Univ.
Blichers Allé 20
Postbox 50
DK-8830 Tjele, Denmark

Per Moldrup
Dep. of Biotechnology, Chemistry and
Environmental Engineering
Aalborg Univ.
Sohngaardsholmsvej 57
DK-9000 Aalborg, Denmark

Emmanuel Arthur
Dep. of Agroecology
Faculty of Science and Technology
Aarhus Univ.
Blichers Allé 20
Postbox 50
DK-8830 Tjele, Denmark

Dorthe Wildenschild
School of Chemical, Biological and
Environmental Engineering
Oregon State Univ.
Corvallis, OR 97331

Marie Eden
Dep. of Agroecology
Faculty of Science and Technology
Aarhus Univ.
Blichers Allé 20
Postbox 50
DK-8830 Tjele, Denmark
and
INRAUMR 1091 Environment and Arable
Crops
INRA-AgroParisTech
F-78850 Thiverval-Grignon, France

Mathieu Lamandé
Dep. of Agroecology
Faculty of Science and Technology
Aarhus Univ.
Blichers Allé 20
Postbox 50
DK-8830 Tjele, Denmark

Hans-Jörg Vogel
Dep. of Soil Physics
Umweltforschungszentrum (UFZ)
Theodor-Lieser-Straße 4
06120 Halle (Saale), Germany

Lis Wollesen de Jonge
Dep. of Agroecology
Faculty of Science and Technology
Aarhus Univ.
Blichers Allé 20
Postbox 50
DK-8830 Tjele, Denmark

The influence of clay content in soil-pore structure development and the relative importance of macroporosity in governing convective fluid flow are two key challenges toward better understanding and quantifying soil ecosystem functions. In this study, soil physical measurements (soil-water retention and air permeability) and x-ray computed tomography (CT) scanning were combined and used from two scales on intact soil columns (100 and 580 cm^3). The columns were sampled along a natural clay gradient at six locations (L1, L2, L3, L4, L5 and L6 with 0.11, 0.16, 0.21, 0.32, 0.38 and 0.46 kg kg^{-1} clay content, respectively) at a field site in Lerbjerg, Denmark. The water-holding capacity of soils markedly increased with increasing soil clay content, while significantly higher air permeability was observed for the L1 to L3 soils than for the L4 to L6 soils. Higher air permeability values observed for 580- than 100-cm^3 soil columns implied a scale effect and relatively greater importance of macropores in convective fluid flow at larger scale. Supporting this, x-ray CT showed that both interaggregate pores and biopores (pores formed by earthworms and plant roots) were present at L1 to L3 in decreasing order, whereas only interaggregate pores were observed at L4 to L6. Macroporosity inferred from x-ray CT to quantify pores >1 mm decreased from 2.9 to 0.1% from L1 to L6. A progressive improvement was observed in the linear relationship (R^2 increasing 0.50–0.95) of air permeability with total air-filled porosity, CT-inferred macroporosity, and CT-inferred limiting macroporosity (minimum macroporosity for any quarter of soil column). The findings of this study show the immense potential in linking x-ray CT-derived soil-pore parameters with classical soil physical measurements for quantifying soil architecture and functions.

Abbreviations: CT, computed tomography.

The preservation and restoration of a beneficial soil structure is important for securing sustainable agriculture production for the future. The importance of soil structure has also been recognized for environmental and groundwater protection because it governs how fast water, greenhouse gases, volatile compounds, chemicals, and pollutants can enter and move through the soil (De Wever et al., 2004; Horn and Smucker, 2005; Jarvis, 2007; de Jonge et al., 2009). Soil type and land use are considered some of the main factors influencing soil structure (Gantzer and Anderson, 2002). In a given region, soil type (e.g., particle size distribution, mineralogy, and pH) acts in the long term (>100 yr) on the whole soil profile, while land use (cropping system and soil faunal activity) has a short-term impact (<1 yr) on soil structure, principally in the top 30 to 40 cm (Lamandé et al., 2011). Among other factors determining soil architecture and structure, the amount and type of clay in a soil has prime importance. This is because the quantity and type of clay minerals present influence soil properties (e.g., cation exchange ca-

pacity and surface area) that are important for soil aggregation (Bronick and Lal, 2004).

Soil physical measurements (e.g., soil water retention and air permeability) have been used in the past as soil structural indicators. Soil water retention is a measure of the water-holding capacity and, indirectly, the pore size distribution of soils. An estimate of the latter can be obtained using the well-known capillary rise equation (Hillel, 1980). Air permeability (k_a) reveals preferential pathways and hence functional soil structure because it is controlled by the macropore space and its connectivity (Moldrup et al., 2001; Kawamoto et al., 2006). Kirkham et al. (1958) suggested that air permeability measurements at field capacity can provide information on changes and differences in soil structure. Arthur et al. (2012) and Schjønning et al. (1994, 2002) used soil water retention and air permeability as soil structural indicators to characterize soil pore structure under different treatments and management conditions.

A step forward in the characterization of soil structure is the development of advanced imaging techniques. X-ray CT is a direct, nondestructive, and noninvasive technique that has been successfully used for three-dimensional examination of soil pore-space geometry. Due to technological advancements in x-ray CT scanning (improved radiometric detectors and cameras and thus spatial resolution) and in the processing of digital imagery (computer capacity and analytical approaches), x-ray CT imaging offers a powerful tool for understanding the soil structure (Taina et al., 2008). Various properties of soil pores and pore networks have been estimated using CT: porosity (Anderson et al., 1990; Rachman et al., 2005; Dowuona et al., 2009), pore size distribution (Luo et al., 2010; Vogel et al., 2010), tortuosity (Peth et al., 2008; Luo et al., 2010), and topology (Vogel et al., 2010; Schlüter et al., 2011). Recently, a few studies have also used x-ray CT to look into preferential pathways (macropores and their connectivity) and their relations to various soil physical processes (Mooney and Morris, 2008; Elliot et al., 2010; Luo et al., 2010). Elliot et al. (2010) used three-dimensional pore characteristics to predict the saturated hydraulic conductivity using Darcy's equation and a modified Poiseuille's equation. Luo et al. (2010) studied quantitative relationships between soil macropore characteristics and preferential flow and transport. They found macroporosity and path number (analyzed using CT) to be the best predictors of saturated hydraulic conductivity. Most of these studies have focused on linking x-ray CT with preferential water flow (saturated hydraulic conductivity), whereas our study focused on preferential air flow (air permeability). The advantage of linking air permeability with x-ray CT is that both of these are nondestructive methods and hence are more suited to reveal soil structure and preferential pathways. Macropores are defined here as the pores >1 mm analyzed using x-ray CT.

The enormous importance of soil structure and its dependence on soil type motivated us to attempt its characterization as a function of soil clay content. The main objective of this study was to quantify comprehensively the role of clay content in the development of soil structure by coupling soil physical measurements (soil water characteristic and air permeability) and x-ray CT. This further gave us the opportunity to establish correlations between x-ray CT derived macropore space parameters (such as macroporosity) and preferential air flow (air permeability).

MATERIALS AND METHODS
Soils Studied

Two sets of intact soil columns of different sizes (100 and 580 cm^3) were sampled for this study. The first set included 30 intact soil samples (60 mm in diameter and 35 mm in height, 100 cm^3) sampled in five replicates at each location (L1–L6) along a naturally occurring clay gradient from Lerbjerg, Denmark. In a second set, 18 large, intact soil cores (100 mm in diameter and 80 mm in height, 580 cm^3) were collected, three from each location along the gradient. All soil samples were sampled from depths below 6 cm in September 2010. After removing the soil-filled cylinder from the field, we trimmed the end faces with a knife and covered them with plastic caps to protect them from mechanical disturbance and evaporation. The undisturbed soil cores were then stored at −2°C until soil physical measurements and x-ray CT scanning could take place. Disturbed soil samples were also collected below the 6-cm depth at the same six locations for textural analysis. The textural analysis of the soils (<2-mm fraction) was performed using a combination of wet-sieving and hydrometer methods. Total organic C was determined by a Leco C analyzer coupled to an infrared CO_2 detector.

Soil Physical Measurements

Soil water retention was measured on the 100-cm^3 soil columns using tension tables (sand boxes) at matric potentials above −10 kPa and pressure plates at matric potentials below −10 kPa. Air permeability was also measured on these soil columns at selected matric potentials (−3, −10, −30, and −100 kPa) using the steady-state method described by Iversen et al. (2001). The pressure gradient was 0.5 kPa, which ensured laminar flow during measurements. The k_a was calculated from Darcy's equation based on the pressure difference across the core.

In a second set of measurements on the 580-cm^3 soil columns, x-ray CT scanning and air permeability measurements were performed after draining them at −30 kPa matric potential. Before measuring k_a, the soil was gently pushed to the edge of the soil columns to minimize the risk of air escaping around the edge of the sample and container. This was done because at lower matric potentials the soil can shrink, leaving a gap at the edge for air to leak through.

X-ray Computed Tomography Analysis

An industrial CT scanner, X-Tek HMX225, was used to scan the 580-cm^3 soil columns. The images were acquired at an energy level of 180 kV and 500 µA, and the resulting images had a voxel size of 0.186 mm. Images were analyzed using ImageJ 1.46a software (Ferreira and Rasband, 2012) to examine the changes in macropore characteristics along the clay gradient. All the images were first cropped to exclude the area outside the soil column.

As a result, the diameter and height of each soil column were reduced to 94 and 74 mm, respectively. After that a median filter with a radius of 2.0, which is a commonly used image-processing method to reduce the noise while preserving the edges (Jassogne et al., 2007), was applied to all images to minimize noise.

The first step in image processing involves the conversion of an image into a bimodal image (pore and solid phase), commonly known as image segmentation. Image segmentation is the crucial step in image analysis because it determines the quality of the final results (Peth et al., 2008). The gray-scale volumes were segmented using a locally adaptive thresholding method proposed by Sauvola and Pietikäinen (2000) and implemented in ImageJ. In this method, the threshold $t(x,y)$ is computed using the mean $m(x,y)$ and standard deviation $s(x,y)$ of the pixel intensities in a w by w window centered around the pixel $p(x,y)$:

$$t(x,y) = m(x,y)\left\{1 + k\left[\frac{s(x,y)}{R} - 1\right]\right\} \qquad [1]$$

where R is the maximum value of the standard deviation ($R = 128$ for a gray-scale eight-bit image) and k is a parameter that takes a positive value 0.5 as proposed by Sauvola and Pietikäinen (2000). The local mean and standard deviation adopt the value of the threshold according to the contrast in the local neighborhood of the pixels. When there is a high contrast in a region of the image, $s(x,y) \approx R$, which results in $t(x,y) \approx m(x,y)$. When the contrast in the local neighborhood is quite low, the threshold $t(x,y)$ goes below the mean value.

After segmentation, macropore characteristics (ignoring pores smaller than five voxels, i.e., approximately <1 mm) including macroporosity, its distribution along the depth of the soil columns, macropore size distribution, surface area, macropore length density, and macropore lengths were analyzed for each soil column using ImageJ software. The ImageJ plug-in 3D viewer (Schmid et al., 2010) was used to visualize the segmented pores in three dimensions for all soil columns. The volume and surface area of macropores in three dimensions were calculated using the ImageJ plug-in Particle Analyzer (Doube et al., 2010). Surface area was calculated by generating the surface mesh for each macropore. Macroporosity was calculated as the ratio of the sum of the volumes of all pore voxels to the volume of the soil column.

The limiting macroporosity, given as the lowest CT-inferred macroporosity of any quarter-length of the soil column, was estimated using the following procedure. Initially, the average macroporosity of the top 20-mm segment of the soil column was determined. After that, one slice (of 0.186-mm thickness) from the top was removed and one slice from the bottom of that 20-mm segment was added each time to average the macroporosity for each successive 20-mm soil column segment. This process was repeated until the bottom of the soil column was reached. The minimum macroporosity found following this procedure for any 20-mm soil column segment while moving from top to bottom was taken as the limiting macroporosity.

The distribution of macroporosity along the depth of the soil column was calculated using the ImageJ Analyze Particles tool. This tool calculates the macroporosity at each scan depth (the mean for each slice) as the ratio of the area of macropores divided by the cross-sectional area of the soil column after cropping.

Soil macropores are three dimensional; therefore, skeletonization of macropores is helpful to quantify the topology and lengths of the pore networks in three dimensions (Capowiez et al., 1998; Peth et al., 2008). The skeleton of a macropores is its centerline, which was generated using the Skeletonize 3D plug-in (Doube et al., 2010) in ImageJ. The three-dimensional medial surface axis thinning algorithm (Lee et al., 1994) is used in this plug-in to find the centerlines of objects in the image. The general idea is to erode the object's surface iteratively until only the skeleton remains. After skeletonization, the Analyze Skeleton plug-in (Doube et al., 2010) in ImageJ was used to quantify the macropore length density and maximum macropore length for each soil column. Macropore length density (cm cm^{-3}) was calculated as the sum of actual lengths of all macropores (ΣL) in a unit volume of soil.

All the soil samples were oven dried for 48 h at 105°C after soil physical measurements and x-ray CT to determine the total porosity and air-filled porosity at specific matric potentials.

Statistical Analysis

A t-test was performed to test for significant differences ($P < 0.05$) in volumetric water contents retained at −10 kPa matric potential (θ_{10}) in the soils from the six locations. Due to deviations from normality of the air permeability measurements at −10 kPa matric potential (k_{a10}), the Mann–Whitney U test was used to test for significant differences ($P < 0.05$) in k_{a10} for soils from six locations. These tests, along with linear regression analysis, were performed using the software Sigma Plot 11.0 (Systat Software Inc.).

RESULTS AND DISCUSSIONS
General Description of Soils

Textural analysis indicated that organic matter remained almost constant, whereas the clay content increased and the sand content decreased from L1 to L6. The clay content varied from 0.112 to 0.463 kg kg^{-1}, silt content from 0.078 to 0.151 kg kg^{-1}, and sand content from 0.810 to 0.386 kg kg^{-1} from L1 to L6. Organic matter content ranged from 0.022 to 0.026 kg kg^{-1} along the clay gradient (Table 1).

Characterization of Soil Structure Along the Clay Gradient
Soil Physical Measurements

Soil-Water Characteristic. The soil-water characteristic was measured (at −1, −3, −5, −10, −30, −50, and −100 kPa matric potentials) on 100-cm^3 soil columns sampled along the clay gradient (average of five replicates at each location) as shown in Fig. 1a. The pF value is defined here as the logarithm of the absolute value of the soil water matric potential in hPa (Schofield, 1935).

Table 1. Soil physical properties along the clay gradient.

Location	Clay	Silt	Sand	Organic matter	USDA Soil type	Total porosity†	Air permeability†
	——————————— kg kg^{-1} ———————————					m^3 m^{-3}	μm^2
L1	0.112	0.078	0.810	0.023	loamy sand	0.44	13.90 a‡
L2	0.161	0.105	0.734	0.023	sandy loam	0.41	2.25 b
L3	0.213	0.115	0.672	0.022	sandy clay loam	0.39	0.85 c
L4	0.318	0.133	0.549	0.022	sandy clay loam	0.46	0.01 d
L5	0.382	0.149	0.469	0.023	sandy clay	0.39	0.19 d
L6	0.463	0.151	0.386	0.023	clay	0.50	0.00 d

† Average for five 100-cm^3 soil samples.

‡ Values followed by different letters are significantly different at $P < 0.05$.

The water-holding capacity of soils at both saturation (pF = 0) and different matric potentials increased with increasing clay content of the soils (from L1 to L6). Total porosity varied from 0.39 to 0.50 in the clay gradient (Table 1), with maximum porosity at L6 (0.463 kg kg^{-1} clay content), whereas minimum porosity was found at L3 (0.213 kg kg^{-1} clay content). This indicates that the soil consisting of balanced proportions of clay, silt, and sand particles (in this case L3) had lower total porosity and higher bulk density. The lower total porosity (higher bulk density) at L5 was might be due to local compaction at the sampling point. A significant difference ($P < 0.05$) was determined in volumetric water contents retained at −10 kPa matric potential (around field capacity) for all six locations (L1–L6) using the t-test. The P value was found to be <0.05 for all locations except L2 and L3, indicating that all locations were significantly different from each other in their water-holding capacities except for L2 and L3 soils (as also marked with letters in Fig. 1a).

The soil-water characteristic has been also used as a traditional measure of the pore size distributions of soils. Figure 1b shows the pore size distributions derived from the soil-water characteristic using the well-known capillary rise equation (Hillel, 1980) for soils along the clay gradient (a ±0.01 error in air-filled porosity can be expected). The widest pore size distribution (having both micro- and macropores) was observed for the L1 soil, and the distribution narrowed as the clay content of the soil increased from L1 to L6. A similar effect of texture on pore size distribution has been reported by Nimmo (2004), who observed a wider pore size distribution for loamy soils than for sandy or clayey soils.

Air Permeability. The gaseous transport parameter (air permeability) has been used in various past studies to characterize the functional soil structure, particularly preferential flow pathways under different treatments (Arthur et al., 2012; Schjønning et al., 1994, 2002). Air permeability (k_a) measured on 100-cm^3 soil samples at −3, −10, −30, and −100 kPa matric potentials was plotted as a function of air-filled porosity (Fig. 2a). The k_a generally increased with increasing air-filled pore space of the soils. Lower air permeability values were observed for soils with increasing clay contents from L1 to L6. Specifically, the low air permeability values (<1 μm^2) observed for the L4 to L6 soils indicates an absence of macropores in these soils. The large scatter in data for the L1 and L2 soils implies the presence of preferential flow pathways in some, but not in all, of the soil columns sampled from the same location. The Mann–Whitney U test was performed to test for significant differences ($P < 0.05$) in k_a values at −10 kPa matric potential (around field capacity) for the L1 to L6 soils. The mean values (for five samples) of air permeability for the L1 to L6 soils are shown in Table 1; the letters indicate their significant differences. This shows that the L1, L2, and L3 soils were significantly different from each other and also from the other soils (L4–L6). The P values found, which were >0.05 for the L4 to L6 soils, implies that they were not significantly different from each other.
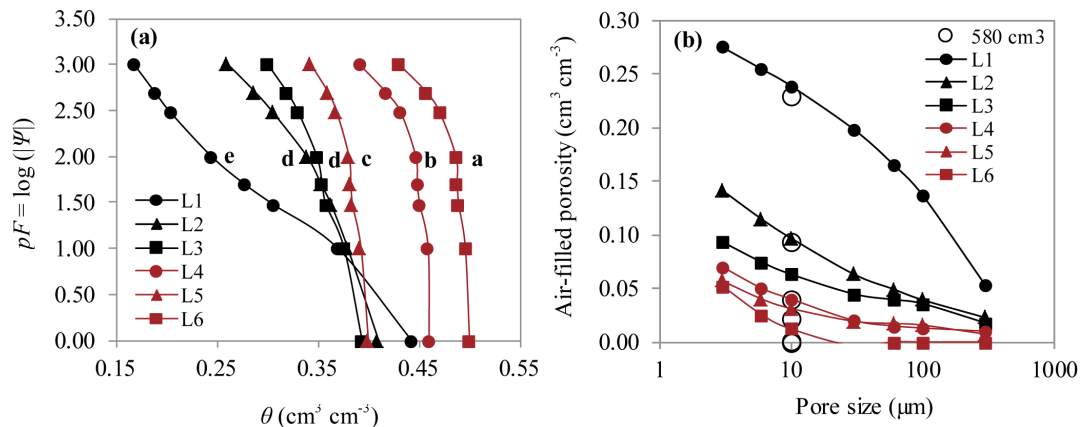

Fig. 1. (a) Measured soil-water characteristic (average of five 100-cm^3 soil samples), where different letters at pF 2.0 denote a significant difference at $P = 0.05$, and corresponding (b) pore size distributions derived from the soil-water characteristic using the capillary-rise equation, where open circles show the comparison for the 580-cm^3 columns.
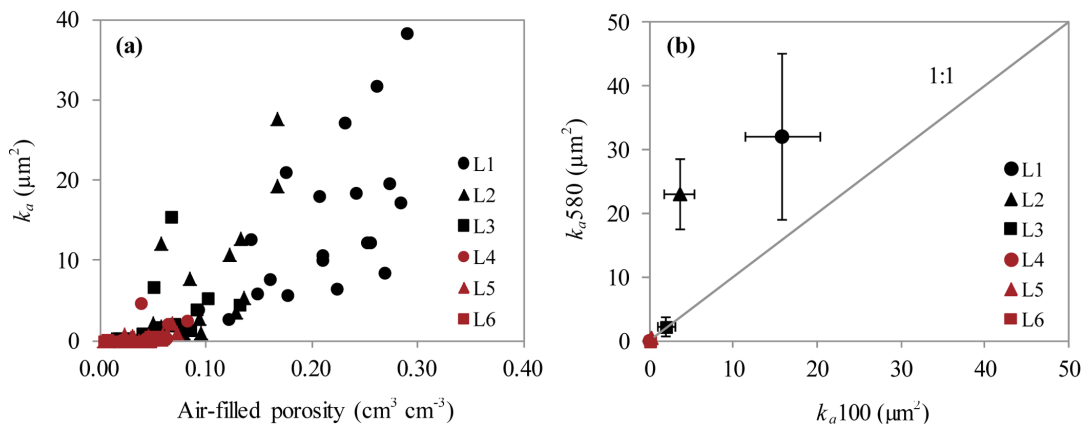
Fig. 2. (a) Air permeability (k_a) measured at −3, −10, −30, and −100 kPa matric potentials plotted as a function of air-filled porosity for 100-cm³ soil columns; (b) comparison between k_a measured at −30 kPa matric potential for 100- and 580-cm³ soil columns sampled along a clay gradient.

Figure 2b shows the comparison between k_a values measured on 100- and 580-cm³ soil columns at −30 kPa matric potential. The air-filled porosities for both soil column sizes were almost the same (corresponding to 10-μm pore size drained) for the L1 to L6 soils, as shown in Fig. 1b. Considerably higher k_a values were observed for the 580-cm³ soil columns than for the 100-cm³ soil columns, particularly for the L1 and L2 soils. No scale effect was observed in k_a values for the L3 to L6 soils, might be due to the absence of macropores in these soils. The scale effect in k_a for the L1 and L2 soils reflects the higher probability of the presence of macropores in large soil columns, which were susceptible to preferential air flow, than in small columns. With this in mind, x-ray CT scanning was performed on the 580-cm³ soil columns to reveal macropore pathways along the clay gradient and their potential relation with convective air flow (i.e., air permeability).

X-ray Computed Tomography

Visualization of Macropores and Macropore Networks. Three-dimensional visualizations of macropores in soil columns (three soil columns from each location, L1–L6) are shown in Fig. 3. The macropores formed by earthworms and roots (biopores) were highly continuous, relatively large, and tubular in shape, whereas the smaller and isolated macropores (vughs and planes) were probably interaggregate macropores such as those formed by freezing–thawing or wetting–drying cycles (Luo et al., 2010). All types of macropores, including biopores and interaggregate macropores, were present in soil columns from L1 to L3 in decreasing order, whereas mainly interaggregate macropores were present in L4 to L6 soils. This suggests that biological (earthworm) activity was present only in the sufficiently aerated soils such as the L1 to L3 soils in this study, while in the L4 to L6 soils only interaggregate macropores formed by freezing–thawing and wetting–drying phenomena were present.

The macropore characteristics (for pores of sizes larger than five voxels, approximately 1 mm) analyzed using x-ray CT for all soil columns including their mean values and standard deviations at each location from L1 to L6 are listed in Table 2.
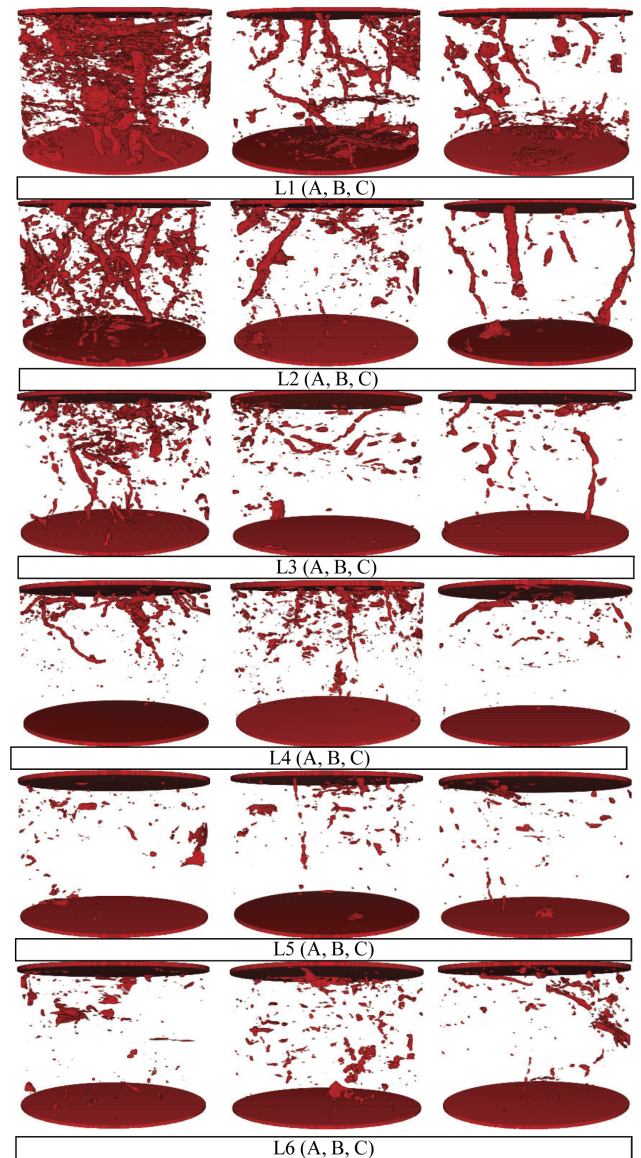

Fig. 3. Three-dimensional visualization (using x-ray computed tomography) of soil macropores in replicates (A, B, and C) of 580-cm³ soil columns sampled along an increasing clay gradient from L1 to L6.

Macropore Size Distribution and Largest Macropore Size. Wider macropore size distributions were observed

Table 2. Macropore characteristics determined from x-ray CT analysis (for pores having size larger than 5 voxels, 1 mm) and air permeability values for respective soil columns (580-cm^3).

Location and soil type	Replicate	Macroporosity	Total surface area	Largest macropore size	Macropore length density	Maximum macropore length	Air permeability
		m^3 m^{-3}	mm^2	mm^3	cm cm^{-3}	mm	μm^2
L1	A	0.023	5829	5209	2.07	38.81	61.87
Loamy sand	B	0.012	3477	1690	0.81	19.89	22.85
	C	0.011	5047	1096	0.64	23.76	11.46
	Mean	0.015 (0.007)†	4784 (1197)	2665 (2223)	1.18 (0.78)	27.49 (10.00)	32.06 (26.44)
L2	A	0.008	2207	1169	0.59	33.03	28.83
Sandy loam	B	0.006	1399	562	0.26	18.47	22.50
	C	0.006	1465	609	0.38	19.24	17.58
	Mean	0.007 (0.001)	1690 (449)	780 (338)	0.42 (0.17)	23.58 (8.19)	22.97 (5.64)
L3	A	0.002	663	180	0.15	33.03	2.16
Sandy clay loam	B	0.004	763	415	0.25	18.14	0.55
	C	0.003	852	365	0.17	15.75	0.42
	Mean	0.003 (0.001)	759 (95)	320 (124)	0.19 (0.06)	22.31 (9.36)	1.04 (0.97)
L4	A	0.003	813	490	0.13	25.93	0.08
Sandy clay loam	B	0.001	348	220	0.10	20.52	0.05
	C	0.001	390	55	0.09	10.46	0.02
	Mean	0.002 (0.001)	517 (257)	255 (220)	0.11 (0.02)	18.97 (7.85)	0.05 (0.03)
L5	A	0.002	636	169	0.16	11.55	1.01
Sandy clay	B	0.004	569	117	0.15	13.32	0.28
	C	0.001	433	257	0.09	12.68	0.03
	Mean	0.002 (0.002)	546 (103)	181 (71)	0.13 (0.04)	12.52 (0.90)	0.44 (0.51)
L6	A	0.001	346	30	0.13	4.74	0.12
Clay	B	0.002	693	143	0.20	8.26	0.09
	C	0.001	741	150	0.15	10.65	0. 01
	Mean	0.001 (0.001)	593 (216)	108 (67)	0.16 (0.04)	7.88 (2.97)	0.07 (0.06)

† Standard deviations in parentheses.

for soil columns sampled from L1, and this narrowed moving from L1 to L6 (Fig. 4). The macroporosity of the soil columns was mainly dominated by macropores >100 mm^3. These larger macropores were probably biopores. The proportion of macroporosity consisting of macropores >100 mm^3 varied from 0.017 m^3 m^{-3} at L1 to 0.00 m^3 m^{-3} at L6. The largest macropore measured 5209 mm^3 at L1 and 30 mm^3 at L6, as given in Table 2.

Macropore Length Density. Macropore length density was calculated from the skeletons of macropores and varied from 2.068 cm cm^{-3} at L1 to 0.125 cm cm^{-3} at L6 (Table 2). The maximum macropore length in the soil columns varied from 38.81 mm at L1 to 4.74 mm at L6 (Table 2). This indicates that no macropore crossed the soil column from top to bottom in any of the soil columns at this x-ray CT resolution.
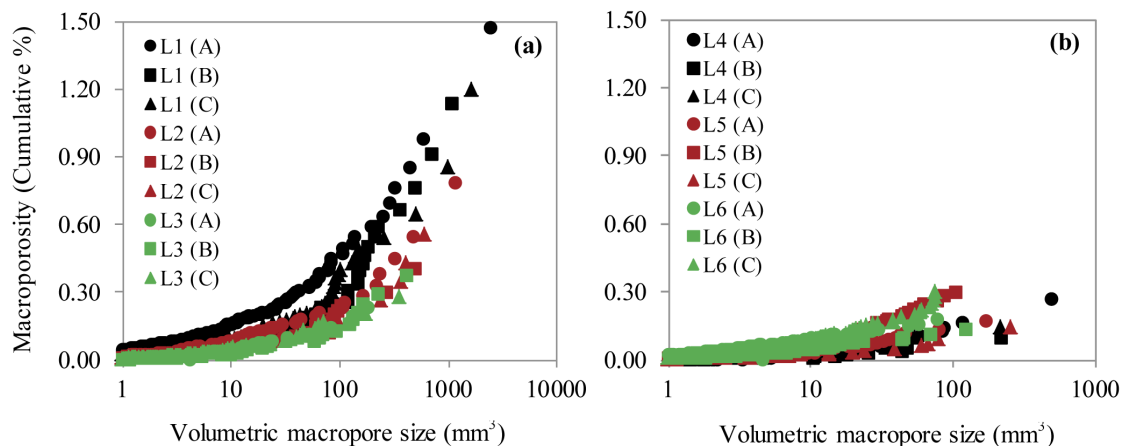

Fig. 4. Cumulative volumetric macropore size distributions for soil column replicates at (a) L1, L2, and L3, and (b) L4, L5, and L6 along an increasing clay gradient.

Macroporosity . The general pattern of macroporosity distribution along the depth of soil columns for L1 to L6 was quite similar, i.e., a decrease with depth (Fig. 5). This indicates that the soil generally became more compact moving down the soil column. Figure 6 shows macroporosity and limiting macroporosity (minimum macroporosity for any quarter of a soil column) plotted as a function of soil clay content from L1 to L6. Macroporosity showed a sharp decrease from L1 to L3 and a modest decrease from L4 to L6. Macroporosity varied from 0.029 m^3 m^{-3} at L1 to 0.001 m^3 m^{-3} at L6. Limiting macroporosity varied from 0.014 m^3 m^{-3} at L1 to 0.00 m^3 m^{-3} at L6 and also showed comparatively less scatter along the clay gradient.

A strong Pearson correlation coefficient was found between macroporosity and the largest macropore size ($r = 0.90$), so the soil column with the highest macroporosity also had the largest macropores. This means that the greater the macroporosity, the greater the chance of macropores being interconnected and forming larger macropores.
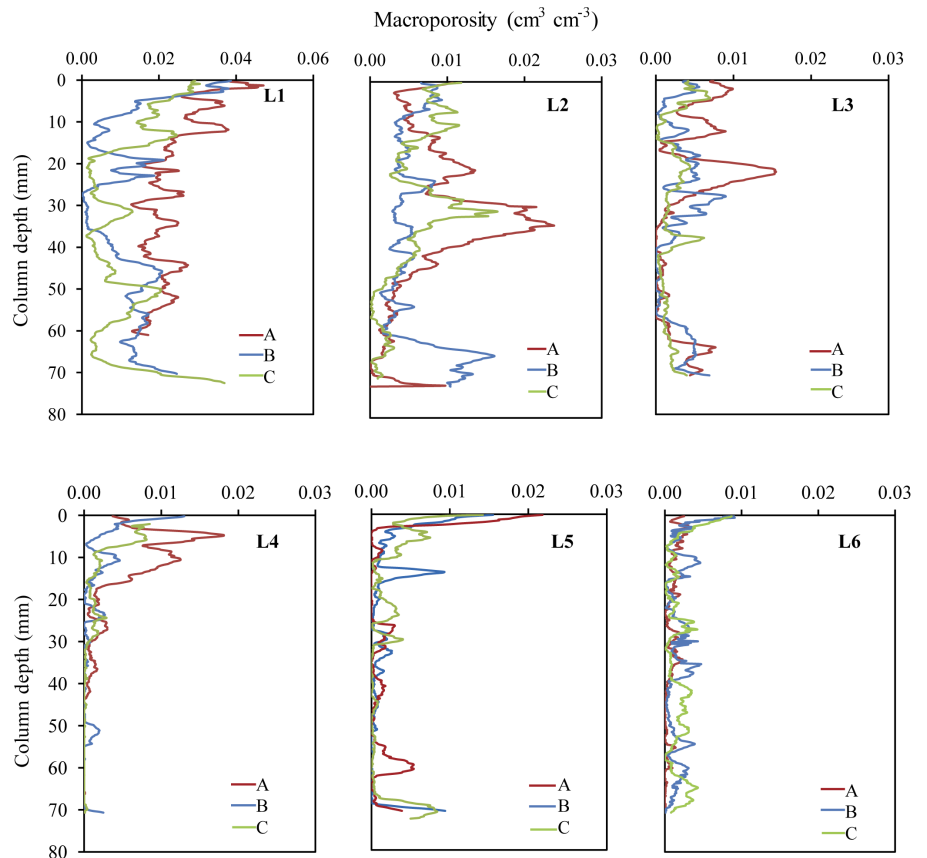

Fig. 5. Macroporosity distribution (analyzed using x-ray computed tomography) along the depth of soil column replicates (A, B, and C) for L1 to L6 along an increasing clay gradient.

Relationship between X-ray Computed Tomography Derived Macroporosity and Air Permeability

Figure 7a shows macroporosity analyzed using x-ray CT plotted as a function of air-filled porosity at −30 kPa matric potential (the matric potential at which the soil columns were scanned). A linear relation among them indicates that x-ray CT detected about 8% (slope of linear regression) of air-filled pores at −30 kPa matric potential. The large scatter of data reflects a large variability in the presence of macropores in the soil columns, irrespective of their air-filled porosities. Air permeability (k_a) is plotted as a function of air-filled porosity in Fig. 7b. Again, a large scatter of data was found; this may be because k_a is mainly controlled by the macropores present in the soil columns rather than the total air-filled pores (Kawamoto et al., 2006). Figures 7c and 7d were plotted showing k_a as a function of macroporosity and limiting macroporosity, respectively. Air permeability showed strong correlations with both macroporosity ($R^2 = 0.88$) and limiting macroporosity ($R^2 = 0.95$). A relatively improved relationship between air permeability and limiting macroporosity was found because macroporosity was not constant along the depth of soil columns (Fig. 5) and hence the column-average macroporosity was not the direct controlling parameter for convective air flow. Linear regressions shown in Fig. 7 were performed only for the L1, L2, and L3 soils while ignoring the

L4 to L6 soils because they were not functional, showing zero air-filled porosity and air permeability values.

Although there was a difference of scales, because x-ray CT could see only the macropores >1 mm in this study (after removing pores smaller than five voxels) while air permeability can "see" (be influenced by) all the air-filled pores down to 10 μm (according to the capillary rise equation at −30 kPa matric potential), a strong relationship was found between the limiting macroporosity derived from x-ray CT and the air permeability. This is because air permeability is mainly controlled by the macropores present in the soil, and therefore macropores analyzed from x-ray CT at
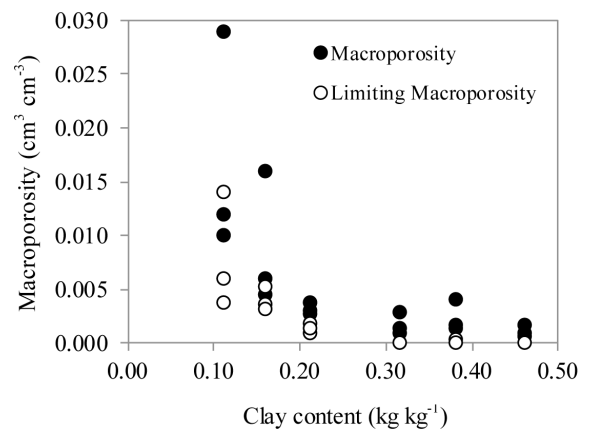

Fig. 6. Macroporosity and limiting macroporosity analyzed using x-ray computed tomography for soil columns plotted along a clay gradient.
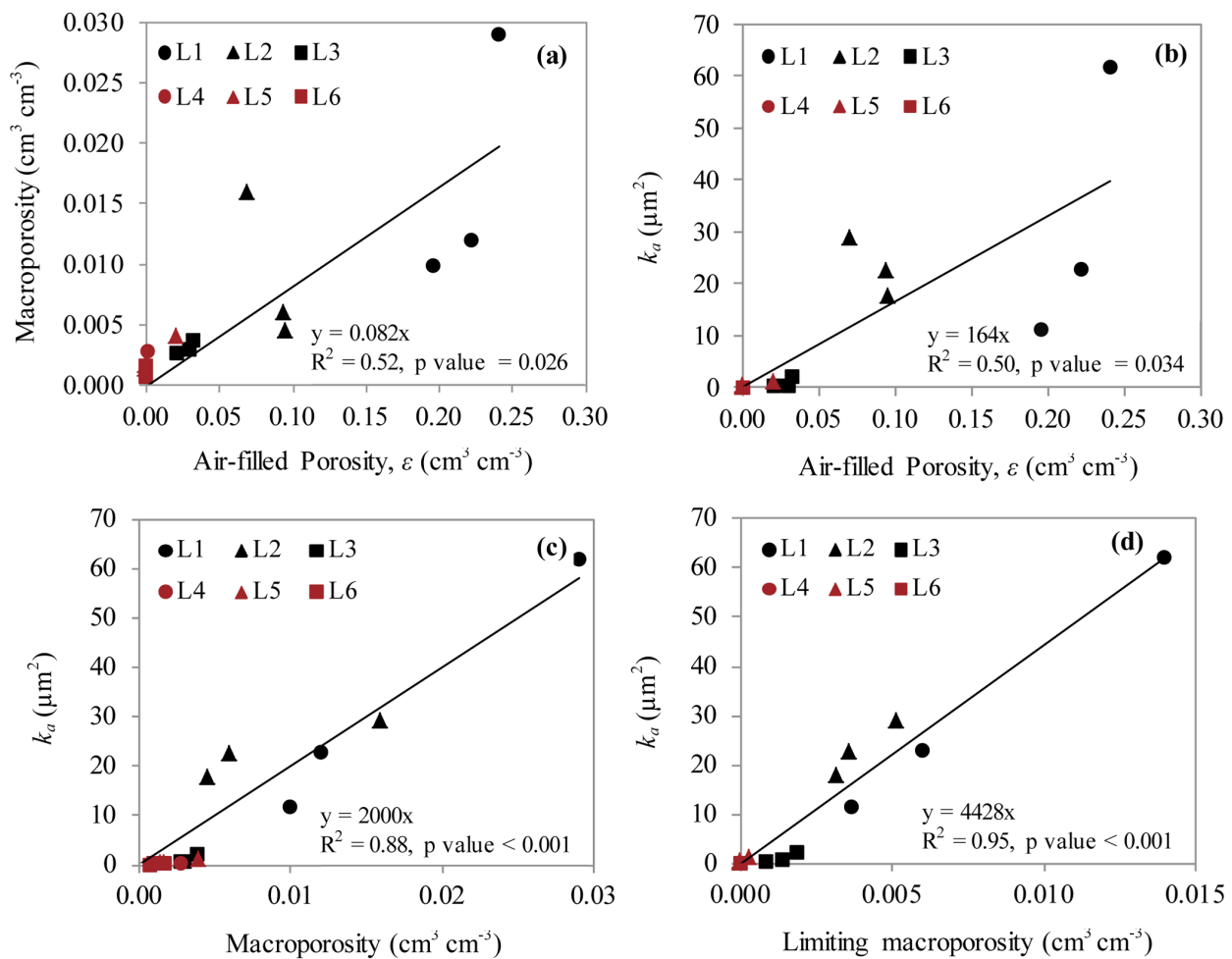
Fig. 7. (a) Macroporosity and (b) air permeability (k_a) plotted as a function of air-filled porosity at −30 kPa matric potential, (c) air permeability plotted as a function of macroporosity, and (d) air permeability plotted as a function of limiting macroporosity for soil columns sampled along an increasing clay gradient from L1 to L6.

this coarse resolution represent all air-filled macropore networks of the soil samples in governing convective fluid transport.

CONCLUSIONS

Soil-pore structural development and functional macropore networks responsible for convective fluid transport were studied by coupling soil physical measurements and x-ray CT on intact soil columns sampled along a naturally occurring clay gradient. The water-holding capacity of the soils increased significantly with the increase in soil clay content from L1 to L6. Significantly higher air permeability values were observed for the L1, L2, and L3 soils than for the L4 to L6 soils. X-ray CT visualization further supported this as large macropores formed by earthworms and plant roots (biopores) were mainly found in soils with clay contents <0.213 kg kg^{-1} (L1–L3). For the soils with higher clay contents (L4–L6), only small and isolated macropores (vughs and planes) formed by freezing–thawing and wetting–drying were observed. Although we could see only 8% of the air-filled pores at −30 kPa matric potential using x-ray CT, macroporosity and limiting macroporosity (macroporosity for any quarter-length of a soil column) were found to be good predictors of air permeability. This is because air permeability is mainly con-

trolled by the macropores present in the soil, and therefore macropore networks found from x-ray CT are representative of the soil samples in governing convective fluid transport. The findings of this study confirmed the huge importance of clay content in soil-pore structure development and further showed a great potential in linking x-ray CT derived soil-pore parameters with soil physical measurements toward revealing and quantifying soil functional structure.

REFERENCES

Anderson, S.H., R.L. Peyton, and C.J. Gantzer. 1990. Evaluation of constructed and natural soil macropores using x-ray computed tomography. Geoderma 46:13–29. doi:10.1016/0016-7061(90)90004-S

Arthur, E., P. Schjønning, P. Moldrup, and L.W. de Jonge. 2012. Soil resistance and resilience to mechanical stresses for three differently managed sandy loam soils. Geoderma 173–174:50–60. doi:10.1016/j.geoderma.2012.01.007

Bronick, C.J., and R. Lal. 2004. Soil structure and management: A review. Geoderma 124:3–22.

Capowiez, Y., A. Pierret, O. Daniel, P. Monestiez, and A. Kretzchmar. 1998. 3D skeleton reconstructions of natural earthworm burrows systems using CAT scan images of soil cores. Biol. Fertil. Soils 27:51–59. doi:10.1007/s003740050399

de Jonge, L.W., P. Moldrup, and P. Schjønning. 2009. Soil infrastructure, interfaces & translocation processes in inner space ("Soil-it-is"): Towards a road map for the constraints and cross-roads of soil architecture and biophysical processes. Hydrol. Earth Syst. Sci. 13:1485–1502. doi:10.5194/hess-13-1485-2009

De Wever, H., D.T. Strong, and R. Merckx. 2004. A system for studying the dynamics of gaseous emissions in response to changes in soil matric potential. Soil Sci. Soc. Am. J. 68:1242–1248. doi:10.2136/sssaj2004.1242

Doube, M., M. Kłosowski, I. Arganda-Carreras, F. Cordelières, R.P. Dougherty, J. Jackson, et al. 2010. BoneJ: Free and extensible bone image analysis in ImageJ. Bone 47:1076–1079. doi:10.1016/j.bone.2010.08.023

Dowuona, G.N.N., I.A. Taina, and R.J. Heck. 2009. Porosity analysis of two acrisols by x-ray computed tomography. Soil Sci. 174:583–593. doi:10.1097/SS.0b013e3181c2a90b

Elliot, T.R., W.D. Reynolds, and R.J. Heck. 2010. Use of existing pore models and x-ray computed tomography to predict saturated soil hydraulic conductivity. Geoderma 156:133–142. doi:10.1016/j.geoderma.2010.02.010

Ferreira, T., and W.S. Rasband. 2012. ImageJ user guide. Natl. Inst. Health, Bethesda, MD. http://imagej.nih.gov/ij/docs/guide/index.html.

Gantzer, C.J., and S.H. Anderson. 2002. Computed tomographic measurement of macroporosity in chisel-disk and no-tillage seedbeds. Soil Tillage Res. 64:101–111. doi:10.1016/S0167-1987(01)00248-3

Hillel, D. 1980. Fundamentals of soil physics. Academic Press, London.

Horn, R., and A.J.M. Smucker. 2005. Structure formation and its consequences for gas and water transport in unsaturated arable and forest soils. Soil Tillage Res. 82:5–14. doi:10.1016/j.still.2005.01.002

Iversen, B.V., P. Schjønning, T.G. Poulsen, and P. Moldrup. 2001. In situ, on site and laboratory measurements of soil air permeability: Boundary conditions and measurement scale. Soil Sci. 166:97–106. doi:10.1097/00010694-200102000-00003

Jarvis, N.J. 2007. A review of non-equilibrium water flow and solute transport in soil macropores: Principles, controlling factors and consequences for water quality. Eur. J. Soil Sci. 58:523–546. doi:10.1111/j.1365-2389.2007.00915.x

Jassogne, L., A. McNeill, and D. Chittleborough. 2007. 3D visualization and analysis of macro- and meso-porosity of the upper horizons of sodic, texture-contrast soil. Eur. J. Soil Sci. 58:589–598. doi:10.1111/j.1365-2389.2006.00849.x

Kawamoto, K., P. Moldrup, P. Schjønning, B.V. Iversen, T. Komatsu, and D.E. Rolston. 2006. Gas transport parameters in the vadose zone: Development and test of power-law models for air permeability. Vadose Zone J. 5:1205–1215. doi:10.2136/vzj2006.0030

Kirkham, D., M.D. Brodt, and L.D. Leiheer. 1958. Air permeability at field capacity as related to soil structure and yield. Meded. Landbouwhogesch. Opzoekingstn. Staat Gent 24:337–391.

Lamandé, M., R. Labouriau, M. Holmstrup, S.B. Torp, M.H. Greve, G. Heckrath, et al. 2011. Density of macropores as related to soil and earthworm community parameters in cultivated grasslands. Geoderma 162:319–326. doi:10.1016/j.geoderma.2011.03.004.

Lee, T.C., R.L. Kashyap, and C.-N. Chu. 1994. Building skeleton models via 3-D medial surface/axis thinning algorithms. Graph. Models Image Process. 56:462–478.

Luo, L.F., H.S. Lin, and S.C. Li. 2010. Quantification of 3-D soil macropore networks in different soil types and land uses using computed tomography. J. Hydrol. 393:53–64. doi:10.1016/j.jhydrol.2010.03.031

Moldrup, P., T. Olesen, T. Komatsu, P. Schjønning, and D.E. Rolston. 2001. Tortuosity, diffusivity, and permeability in the soil liquid and gaseous phases. Soil Sci. Soc. Am. J. 65:613–623. doi:10.2136/sssaj2001.653613x

Moody, S.J., and C. Morris. 2008. A morphological approach to understanding preferential flow using image analysis with dye tracers and x-ray computed tomography. Catena 73:204–211. doi:10.1016/j.catena.2007.09.003

Nimmo, J.R. 2004, Porosity and pore size distribution. In: D. Hillel, editor-in-chief, Encyclopedia of soils in the environment. Vol. 3. London, Elsevier. p. 295–303.

Peth, S., R. Horn, F. Beckmann, T. Donath, J. Fischer, and A.J.M. Smucker. 2008. Three-dimensional quantification of intra-aggregate pore-space features using synchrotron-radiation-based microtomography. Soil Sci. Soc. Am. J. 65:613–623. doi:10.2136/sssaj2007.0130

Rachman, A., S.H. Anderson, and C.J. Gantzer. 2005. Computed-tomographic measurement of soil macroporosity parameters as affected by stiff-stemmed grass hedges. Soil Sci. Soc. Am. J. 69:1609–1616. doi:10.2136/sssaj2004.0312

Sauvola, J., and M. Pietikäinen. 2000. Adaptive document image binarization. Pattern Recognit. 33:225–236. doi:10.1016/S0031-3203(99)00055-2

Schlüter, S., U. Weller, and H.-J. Vogel. 2011. Soil structure development including seasonal dynamics in a long-term fertilization experiment. J. Plant Nutr. Soil Sci. 174:395–403. doi:10.1002/jpln.201000103

Schjønning, P., B. Christensen, and B. Carstensen. 1994. Physical and chemical properties of a sandy loam receiving animal manure, mineral fertilizer or no fertilizer for 90 years. Eur. J. Soil Sci. 45:257–268. doi:10.1111/j.1365-2389.1994.tb00508.x

Schjønning, P., L.J. Munkholm, P. Moldrup, and O.H. Jacobsen. 2002. Modelling soil pore characteristics from measurements of air exchange: The long-term effects of fertilization and crop rotation. Eur. J. Soil Sci. 53:331–339. doi:10.1046/j.1365-2389.2002.00438.x

Schmid, B., J. Schindelin, A. Cardona, M. Longair, and M. Heisenberg. 2010. A high-level 3D visualization API for Java and ImageJ. BMC Bioinformatics 11:274. doi:10.1186/1471-2105-11-274

Schofield, R.K. 1935. The pF of the water in soil. In: E.M. Crowther et al., editors, Transactions of the 3rd International Congress of Soil Science, Oxford, UK. 30 July–7 Aug. 1935. Vol. II. Thomas Murby & Co., London. p. 37–48.

Taina, I.A., R.J. Heck, and T.R. Elliot. 2008. Application of x-ray computed tomography to soil science: A literature review. Can. J. Soil Sci. 88:1–20. doi:10.4141/CJSS06027

Vogel, H.-J., U. Weller, and S. Schlüter. 2010. Quantification of soil structure based on Minkowski functions. Comput. Geosci. 36:1236–1245. doi:10.1016/j.cageo.2010.03.007